Enhanced CeO_2 oxygen defects decorated with $AgInS_2$ quantum dots form an S-scheme heterojunction for efficient photocatalytic selective oxidation of xylose

Aohua Li[a], Jiliang Ma[a *], Min Hong[b] and Runcang Sun[a *]

[a] *Liaoning Key Lab of Lignocellulose Chemistry and BioMaterials, Liaoning Collaborative Innovation Center for Lignocellulosic Biorefinery, College of Light Industry and Chemical Engineering, Dalian Polytechnic University, Dalian 116034, China*

[b] *Centre for Future Materials, University of Southern Queensland, Springfield Central Queensland, 4300, Australia*

*Corresponding authors' E-mail address**:** jlma@dlpu.edu.cn (Jiliang Ma) and rcsun3@dlpu.edu.cn (Runcang Sun), Tel.: +86-0411-86323652, Fax: +86-0411-86323652

ABSTRACT

S-scheme heterojunctions have become an emerging type of effective photocatalysts to convert biomass. However, there are few reports on the synergistic S-type heterojunction and oxygen vacancy enhanced photocatalytic biomass conversion. Here, an $AgInS_2$@CeO_2-x S-scheme heterojunction photocatalyst with abundant oxygen vacancies was developed through a simple thermal and mild annealing process, allowing for the simultaneous production of xylonic acid and CO. Under visible light, the xylonic acid yield and CO evolution rate reached 60.0% and 3689.9 μmol g^{-1} h^{-1}, respectively, through the decomposition of xylose. It was found that the S-scheme staggered band structure could improve sunlight utilization, increase the reduction power of photogenerated electrons, and enhance the separation and transfer of photogenerated charge carriers. Furthermore, oxygen vacancies on the surface of CeO_2 for $AgInS_2$@CeO_2-x heterojunction can suppress the recombination of generated electrons and holes. This study offers a promising approach for designing artificial photosynthetic systems to promote photocatalytic biomass conversion.

Keywords: S-scheme heterojunction; Oxygen vacancies; Xylonic acid; CO; Photocatalytic biorefinery;

1. Introduction

As the only renewable carbon source in nature, biomass stores solar energy and carbon through photosynthesis [1, 2]. The abundance of chemicals and fuels are converted from biomass. Photocatalysis is a promising strategy to produce value-added chemicals, which has attracted increasing attention [3, 4]. Various photocatalytic processes and photocatalysts have been developed for biomass conversion to produce hydrogen, liquid fuels, and other chemicals [5-7]. Xylonic acid, which is a biomass-derived acid, was listed by the US Department of Energy as one of the thirty most potential compounds [8]. Meanwhile, photocatalytic biorefinery is an important pathway to produce xylonic acid [9].

Compared with traditional high-temperature chemical and biological methods, photocatalytic technology has diversified advantages, such as mild reaction conditions, high efficiency, and low energy consumption [10]. For example, Liu et al. employed carbon aerogel material (*a*-TiO_2@MC) by anchoring chitosan and sodium carboxymethylcellulose. The xylonic acid yield reached its maximum (52.26%) from xylose under visible light irradiation [11]. Nevertheless, the above research only focuses on the liquid products in the reaction without gas products. In previous reports, Wang et al. dispersed Cu on titanium oxide nanorods for the selective conversion of biomass-derived sugars into CO [5]. Zhang et al. reported 1213.88 μmol g^{-1} h^{-1} CO evolution during the photocatalytic process of producing xylonic acid from xylose using CIS/GO@3D-OMA photocatalyst [12]. These reported research findings suggest that the co-production of xylonic acid and CO in the photocatalytic biorefinery process is a feasible process, which improves atomic utilization. To achieve this, it is essential to design a photocatalyst with high selectivity and activity.

In the past decades, rare earth metal oxide materials have shown tremendous capabilities in efficient and cost-effective photocatalysis for various reactions due to their unique physical and chemical properties [13]. Cerium oxide (CeO_2) is regarded as one of the most promising photocatalysts, due to high structural stability, low cost, and excellent redox ability [14, 15]. The rich surface chemical features of CeO_2 including

Lewis acidic site, Lewis basic site, Bronsted acidic site, and oxygen vacancy provide an ideal platform to understand the influence of adsorption behavior on the catalytic performance of CeO_2-based heterogeneous catalysts. Oxygen vacancies and Ce^{3+} ions in ceria can improve oxygen gas adsorption and activation as well as oxygen self-diffusion in the lattice of nonstoichiometric ceria, benefiting the redox process and catalytic reaction [16]. Serving as electron donors, oxygen vacancies improve electron migration in the photocatalytic process [17, 18]. The formation of oxygen vacancies can be controlled by rationally tunning thermal-treatment temperature and oxygen partial pressure, doping elements and content, synthesis methods, surface stress, and electrical field [16]. Nevertheless, the wide bandgap and low visible light utilization hinder CeO_2 as efficient photocatalysts [19, 20]. Additionally, a single photocatalyst cannot reserve both the strong oxidation ability of holes and the strong reduction ability of electrons due to band structure limitations [21].

It is challenging to develop an efficient photocatalytic system that simultaneously exhibits visible light responses, effective charge separation and strong redox capabilities. In this regard, constructing an S-scheme heterojunction composed of reduction photocatalysts (RP) and oxidation photocatalysts (OP) is a promising strategy for improving photocatalytic efficiency. S-scheme heterojunction has proven to be a superior junction system with a strong built-in electric field, which facilitates the separation of electron-hole pairs and maintains their high redox ability [22]. When RP and OP come into contact without light irradiation, band bending and an internal electric field appear at the interface of the two semiconductor contacts. Upon light irradiation, electrons are excited to form electron-rich and hole-rich regions in RP and OP, respectively. Driven by an internal electric field, the photo-generated electrons on the conduction band (CB) of OP consume holes on the valence band (VB) of RP. Simultaneously, photo-generated electrons and holes with strong redox abilities are increasingly retained on the CB of RP and the VB of OP, ensuring the high redox ability of S-scheme heterojunctions [23, 24].

One typical example to demonstrate the highly efficient photocatalyst of S-scheme heterojunctions is Ni@6MOF/$BiVO_4$, prepared using an H-bonding-induced assembly

process [25]. The CO_2 photo-conversion of Ni@6MOF/$BiVO_4$ was reported to be 66 times higher than that of $BiVO_4$ nanoparticles in pure water, because of the favorable charge separation under the positive influence of S-scheme heterojunctions. Moreover, You et al. developed a hollow structured S-scheme heterojunction named h-ZnSe/Pt@TiO_2 to produce H_2 and formic acid in pure water. The productivities of H_2 and formic acid reached 1858 and 372 μmol g^{-1} h^{-1}, respectively, for over 300 h [26].

$AgInS_2$ quantum dots (QDs), typical reduction photocatalysts (RP), have garnered increasing interest in the field of photocatalytic degradation, originating from $AgInS_2$ featured by high chemical stability, tunable band structure and excellent visible light response [27, 28]. Furthermore, QDs exhibit better electron-hole pairs separation compared with bulk materials due to the short electron-hole diffusion distance [29, 30]. Previous studies have demonstrated that constructing heterojunctions via incorporating pure $AgInS_2$ with additional compatible photocatalysts can effectively improve the photocatalytic activity [31].

In this study, we have devised a 0D/3D S-scheme heterojunction involving CeO_2 adorned with $AgInS_2$ QDs to improve the photocatalytic efficiency using straightforward two-step hydrothermal and mild annealing processes. Electron paramagnetic resonance (EPR) analysis has confirmed the increased oxygen vacancies in the successfully constructed S-scheme heterojunction, which serve as electron donors to favor the photocatalytic performance. Moreover, staggered band structures with distinct Fermi levels between $AgInS_2$ QDs and CeO_2 effectively enhances charge separation. Accordingly, our S-scheme heterojunction yields superior photocatalytic performance, resulting in the highly efficient production of xylonic acid (60.0%) and CO (3689.9 μmol g^{-1} h^{-1}). The underlying charge transfer mechanism in S-scheme is elucidated through *in-situ* X-ray photoelectron spectroscopy (*in-situ* XPS) and Kelvin probe force microscopy (KPFM) spectra. This study offers a promising approach for developing defect-rich S-scheme photocatalysts for the production of biomass-derived chemicals and fuels via photocatalytic biomass refining.

2. Experimental section

2.1. Preparation of CeO_2.

First, 4 mL of *N*-butyl silicate, 60 mL of ethanol, and 9 mL of ammonia solution were mixed with 100 mL of deionized water, followed stirring for 1 h. The mixed solution was centrifugated at 5,000 rpm for 10 min to obtain SiO_2. The collected powder was dried at 60 ºC for 8 h to obtain SiO_2. Afterward, 0.15 g of SiO_2 were added to 30 mL of ethanol and sonicated for 30 min to obtain a homogeneous suspension, referred to as suspension A. Next, 2.6 g of $Ce(NO)_3 \cdot 6H_2O$ and 0.8 g of urea were dissolved in 50 mL of deionized water to create solution B. Suspension A and solution B were thoroughly mixed in a stainless-steel autoclave and treated at 160 ºC for 8 h in an Ar atmosphere. At the end of the reaction, the white powder of $SiO_2@CeO_2$ was obtained after centrifugation and drying. Finally, 2 g of $SiO_2@CeO_2$ was added to 80 mL of 2 M KOH and treated in a beaker using a water bath at 80 ºC for 2 h. These steps should be repeated six times. After drying at 60 ºC for 4 h, the powder was annealed at 600 ºC for 2 h in an air atmosphere to obtain the yellow powder of CeO_2.

2.2. Preparation of $AgInS_2$ QDs.

1.1678 g of indium acetate, 12.2928 g of glutathione, 0.6748 g of silver nitrate, and 10 mL of an 8 mM Na_2S solution were added into 250 mL of deionized water. The pH of resulting mixture was adjusted to 8.0 using a concentrated NaOH solution. Subsequently, the solution was treated in a round-bottom flask in an oil-bath at 100 ºC for 3.5 h. After chilling to the room temperature, an excess of ethanol was added to the solution to precipitate $AgInS_2$ QDs. Next, the mixture was centrifugated at 8,000 rpm for 10 min to obtain a black precipitate. The black precipitate was then washed several times with deionized water and ethanol. Finally, the black powder $AgInS_2$ QDs were obtained through the process of drying.

2.3. Preparation of $AgInS_2@CeO_2$-x photocatalysts.

0.5 g of CeO_2 and a specific amount of $AgInS_2$ QDs were added into 10 mL of

deionized water. The mixture was evaporated to dryness at 90 °C to give a dry powder. Subsequently, the blend of CeO_2 and $AgInS_2$ QDs was annealed at 200 °C for 20 min in an Ar atmosphere to produce the $AgInS_2$@CeO_2-x heterostructure. The mass ratios of $AgInS_2$ QDs to CeO_2 were 5%, 10%, 20%, and 30%, respectively. Correspondingly, the resulting materials were labeled as $AgInS_2$@CeO_2-5, $AgInS_2$@CeO_2-10, $AgInS_2$@CeO_2-20, and $AgInS_2$@CeO_2-30, respectively.

2.4. Photocatalytic co-production of xylonic acid and CO from xylose

Typically, 10 mg of $AgInS_2$@CeO_2-x and 200 mg of xylose were added into 20 mL of a KOH aqueous solution. The photocatalytic co-production of CO and xylonic acid was carried out under visible light irradiation using the Perfectlight PCX 50C multi-channel photocatalytic reaction system, with varying reaction temperatures, irradiation times, and alkali concentrations. Finally, the resulting liquid product and the generated CO were analyzed using high-performance liquid chromatography (HPLC) and gas chromatography (GC), respectively.

2.5. Poisoning experiments.

Typically, 10 mg of $AgInS_2$@CeO_2-20, 200 mg of xylose and 20 mmol of sacrificial agents (tryptophan (Trp), *p*-phthalic acid (PTA), *p*-benzoquinone (BQ), and ethylenediaminetetraacetic acid (EDTA)) were added into 20 mL of a 0.1 M KOH solution. The reaction was conducted under visible light irradiation at approximately 60 °C for 1 h. Finally, the resulting liquid product and the generated CO were analyzed using the methods mentioned above.

2.6. Recycling experiments.

The methods of recycling experiments were the same as described above. In each cycle, 10 mg of $AgInS_2$@CeO_2-20 and 200 mg of xylose was added into 20 mL of a 0.1 M KOH solution. The reaction was irradiated by visible light at ~ 60 °C for 1 h. The obtained liquid product and the generated CO were analyzed using the methods

mentioned previously. At the end of each cycle, the system was centrifugated at 5000 rpm for 10 min to recover $AgInS_2$@CeO_2-20. Meanwhile, HPLC and GC were used to analyze the produced liquid product and CO for each cycle.

3. Results and discussion

3.1 Catalyst Preparation and Characterizations.

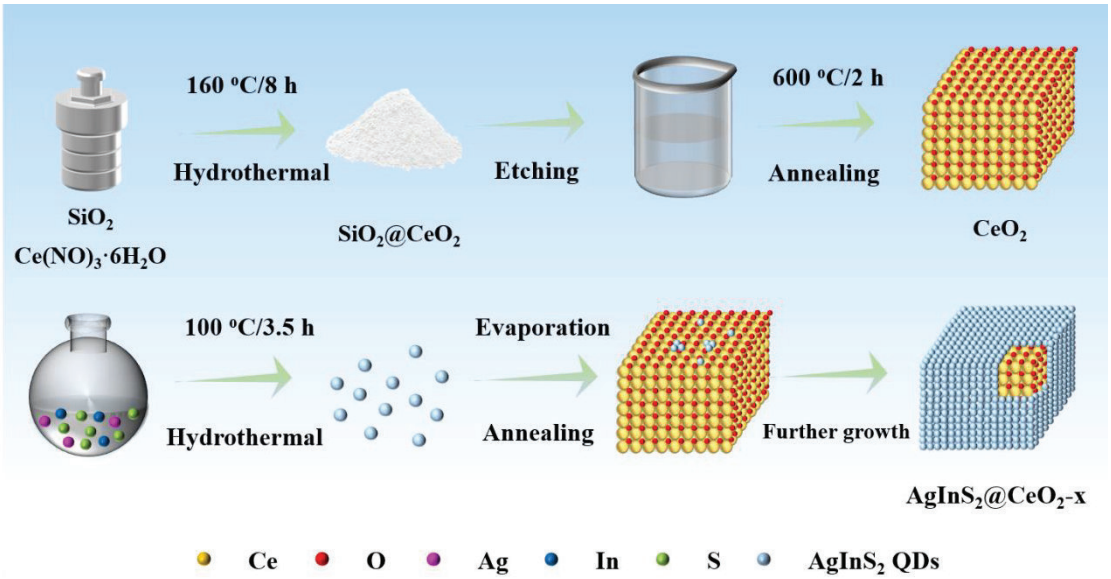

Fig. 1. The schematic illustration of fabricating $AgInS_2$@CeO_2-x.

Fig. 1 illustrates the two-step hydrothermal and mild annealing processes for preparing $AgInS_2$@CeO_2-x, involving the loading of $AgInS_2$ QDs to form a tightly bonded heterojunction. Photocatalysts with varying mass ratios of $AgInS_2$ QDs and CeO_2 were prepared and named $AgInS_2$, CeO_2-x, $AgInS_2$@CeO_2-5, $AgInS_2$@CeO_2-10, $AgInS_2$@CeO_2-20, and $AgInS_2$@CeO_2-30, respectively. The microscopic morphologies of the prepared samples were investigated using scanning electron microscopy (SEM) and transmission electron microscopy (TEM). Fig. 2A, 2B and S1A depict that the $AgInS_2$@CeO_2-20 shows a hexahedral block structure formed by arrangement of nanospheres. CeO_2 exhibits a layered block like structure with nanospheres arrangement (Fig. S1B and S1C). Fig. S2 displayed the N_2 sorption isotherms of CeO_2, and SiO_2@CeO_2. All of them exhibited type IV isotherm patterns, suggesting the existence of numerous mesopores in these samples. Compared to the SiO_2@CeO_2 (15.7 m^2/g), the specific surface area (28.9 m^2/g) of CeO_2 was greatly enhanced after the removal of SiO_2, which created more mesopores. The enhanced specific surface area could facilitate the diffusion of xylose into photocatalysts. As

shown in Fig. S3, the presence of Ag, In, and S elements was detected in the $AgInS_2$@CeO_2-20, confirming the successful introduction of $AgInS_2$ QDs.

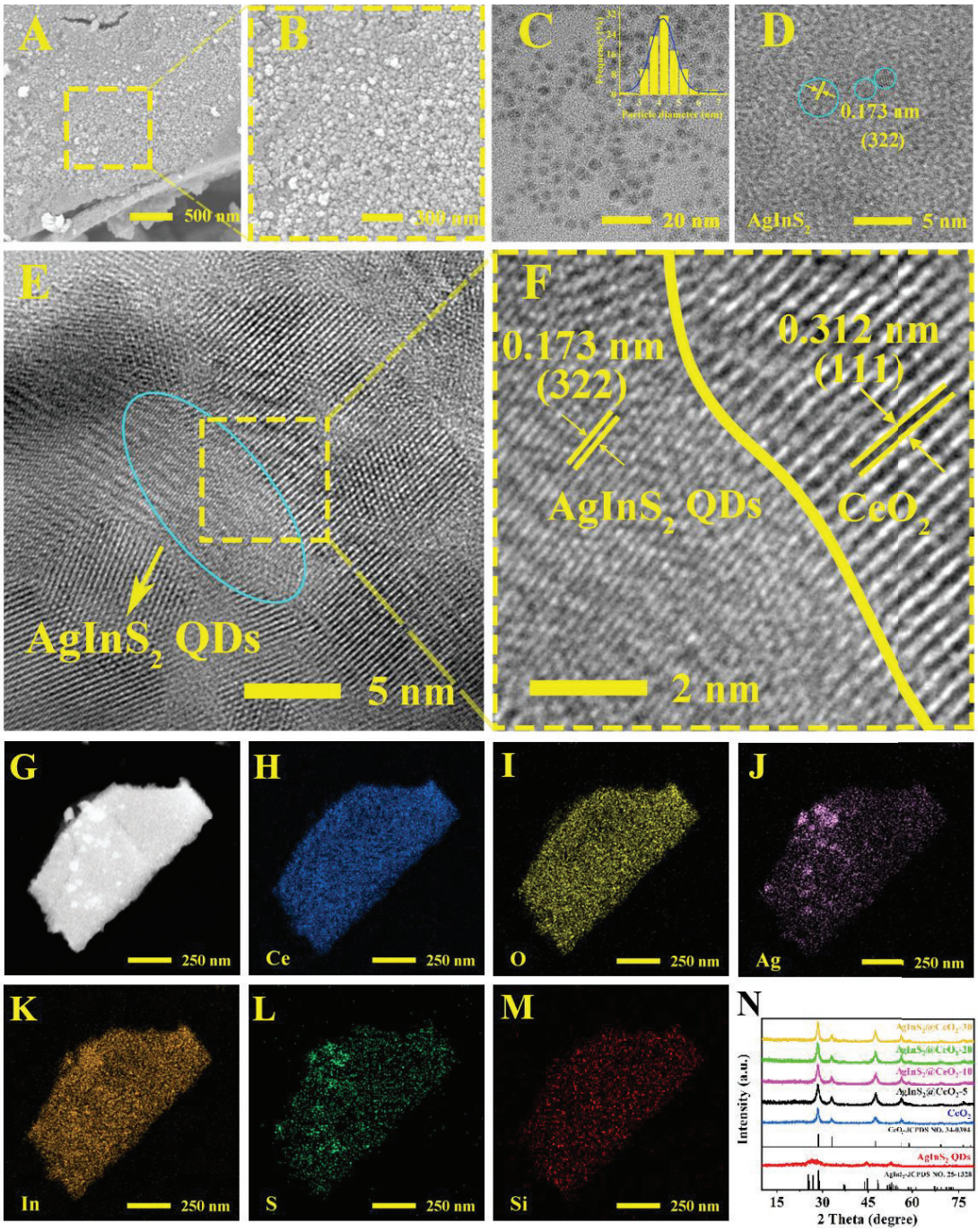

Fig. 2. SEM images of $AgInS_2$@CeO_2-20 (A and B). TEM image (C) and HRTEM image (D) of $AgInS_2$ QDs. HRTEM images of $AgInS_2$@CeO_2-20 (E and F). The HADDF-STEM image (G) and the EDX mapping images (H-M) of $AgInS_2$@CeO_2-20. The XRD patterns of CeO_2, $AgInS_2$ QDs, and $AgInS_2$@CeO_2-x (N).

TEM image and high-resolution TEM (HRTEM) images of $AgInS_2$ QDs (Fig. 2C and 2D), its size ranges from 3 to 5 nm [32], while its lattice fringes with *d*-spacing of 0.173 nm correspond to the (322) crystal plane of $AgInS_2$ QDs. Furthermore, HRTEM image (Fig. 2E) of $AgInS_2$@CeO_2-20 confirm the formation of heterogeneous structures, identifying the crystalline phases of $AgInS_2$ QDs and CeO_2, respectively. The *d*-spacing value of 0.173 nm in $AgInS_2$ QDs corresponds to the (322) crystal plane, while the 0.312 nm *d*-spacing in CeO_2 corresponds to the (111) crystal plane [33] (Fig. 2F). To further investigate the loading of $AgInS_2$ QDs, energy-dispersive X-ray spectroscopy (EDX) analysis was performed, confirming the successful introduction of all elements (Ag, In, and S) from the $AgInS_2$ QDs (Fig. 2J-L). Fig. 2N presents X-ray diffraction (XRD) patterns for CeO_2, $AgInS_2$ QDs, $AgInS_2$@CeO_2-5, $AgInS_2$@CeO_2-10, $AgInS_2$@CeO_2-20, and $AgInS_2$@CeO_2-30. Pristine CeO_2 exhibits four typical diffraction peaks at 28.4°, 33.0°, 47.4°, and 56.4°, attributed to the (111), (200), (220), and (311) crystal planes of CeO_2 (JCPDS No.34-0394), respectively [33]. The diffraction peaks of $AgInS_2$ QDs match those of standard orthorhombic $AgInS_2$ crystals (JCPDS No.25-1328) [34]. Notably, no diffraction peaks of $AgInS_2$ are observed in the XRD pattern of $AgInS_2$@CeO_2-x due to the low crystallinity of $AgInS_2$ QDs [35].

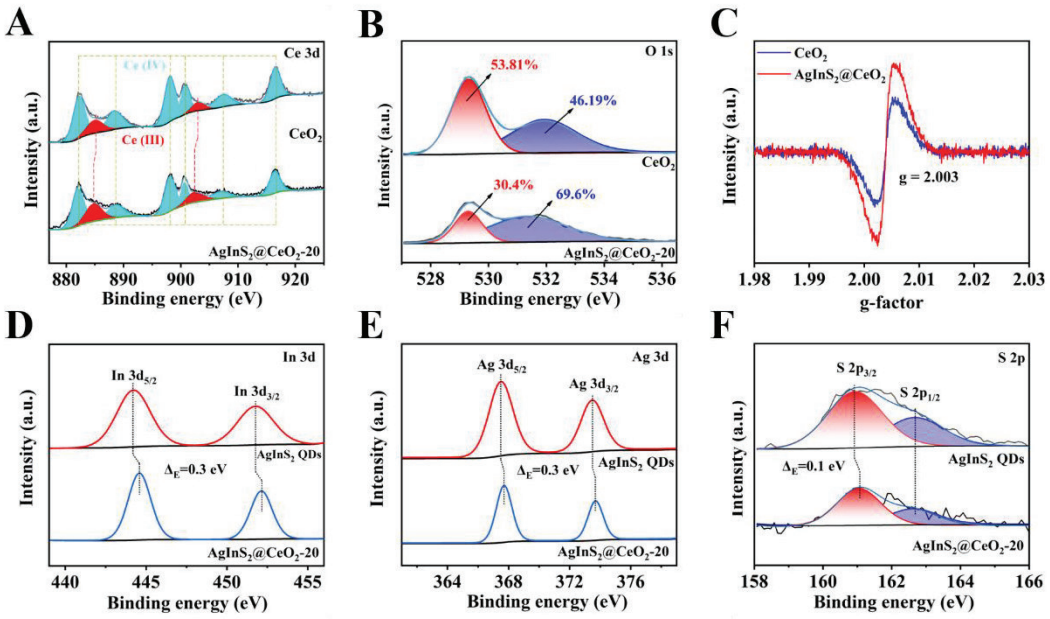

Fig. 3. High-resolution ex-situ XPS spectra of Ce 3d (A) and O 1s (B) for CeO_2 and

$AgInS_2$@CeO_2-20, along with Ag 3d (D). EPR spectra of CeO_2 and $AgInS_2$@CeO_2-20 (C). High-resolution XPS spectra of In 3d (E) and S 2p (F) for $AgInS_2$ QDs and $AgInS_2$@CeO_2-20.

X-ray photoelectron spectroscopy (XPS) was conducted to further investigate chemical composition and state of elements in the prepared photocatalysts. The XPS survey spectrum of $AgInS_2$@CeO_2-20 confirmed the presence of Ce, O, Ag, In, and S (Fig. S4). As shown in Fig. 3A, several peaks in CeO_2, located at 916.5 eV, 907.4 eV, 900.7 eV, 898.1 eV, 888.8 eV, and 882.3 eV, were attributed to Ce (IV) species, while the peaks at 902.4 eV and 884.9 eV in CeO_2 were associated with Ce (III) species [36]. Notably, after the heterojunction was formed between $AgInS_2$ QDs and CeO_2, the binding energy of Ce (III) species in the $AgInS_2$@CeO_2-20 complex decreased as compared with CeO_2. This suggests that in the absence of illumination, the CeO_2 acts as an e^- acceptor in $AgInS_2$@CeO_2-20 complex. Interestingly, the peak area ratios of Ce (III) to Ce (IV) in CeO_2 and $AgInS_2$@CeO_2-20 were calculated to be 5.28% and 36.84%, respectively. A high ratio of Ce (III) to Ce (IV) is advantageous for creating abundant oxygen vacancies, thereby enhancing photocatalytic activity [37]. Oxygen vacancies can function as e^- or h^+ capture sites, improving charge separation by restraining the recombination of h^+-e^- pairs [38]. The O 1s spectrum of CeO_2 can be fitted with two peaks at 532.0 eV and 529.3 eV, attributing to surface oxygen vacancies (O_v) and lattice oxygen (O_{lat}), respectively (Fig. 3B) [39, 40]. Evidently, the peak area of O_v species in $AgInS_2$@CeO_2-20 (69.6%) is higher than that in CeO_2 (46.19%), primarily due to the higher concentration of Ce (III) species on the $AgInS_2$@CeO_2-20 leading to the formation of oxygen vacancies. To further confirm the existence of O_v, electron paramagnetic resonance (EPR) technology was employed (Fig. 3C). Both the CeO_2 and $AgInS_2$@CeO_2-20 sample exhibited EPR signals centered at g = 2.003, indicative of e^- trapped at O_v. The noticeable increase in the signal peak intensity of $AgInS_2$@CeO_2-20 suggests an increase in O_v, implying the role of mild annealing [41]. The Ag 3d spectrum in $AgInS_2$ QDs reveals two peaks at 373.7 eV and 367.7 eV, attributed to Ag $3d_{3/2}$ and Ag $3d_{5/2}$, respectively (Fig. 3D). As displayed in Fig. 3E, the peaks at 452.2

eV and 444.6 eV in the In 3d spectrum of $AgInS_2$ QDs correspond to In $3d_{3/2}$ and In 3d $d_{5/2}$ for In^{3+}, respectively [42]. The S 2p spectrum of $AgInS_2$ QDs can be deconvoluted into two characteristic peaks at 162.5 eV and 160.9 eV (Fig 2F), assigning to S $2p_{1/2}$ and S $2p_{3/2}$ for S^{2-}, respectively [43]. Remarkably, in comparison to $AgInS_2$, the binding energies of Ag 3d, In 3d and S 2p in $AgInS_2$@CeO_2-20 increased, which may be attributed to the interfacial interactions between $AgInS_2$ QDs and CeO_2 [44]. These results further confirm the successful preparation of $AgInS_2$@CeO_2-20.

3.2 Optical and electrical properties.

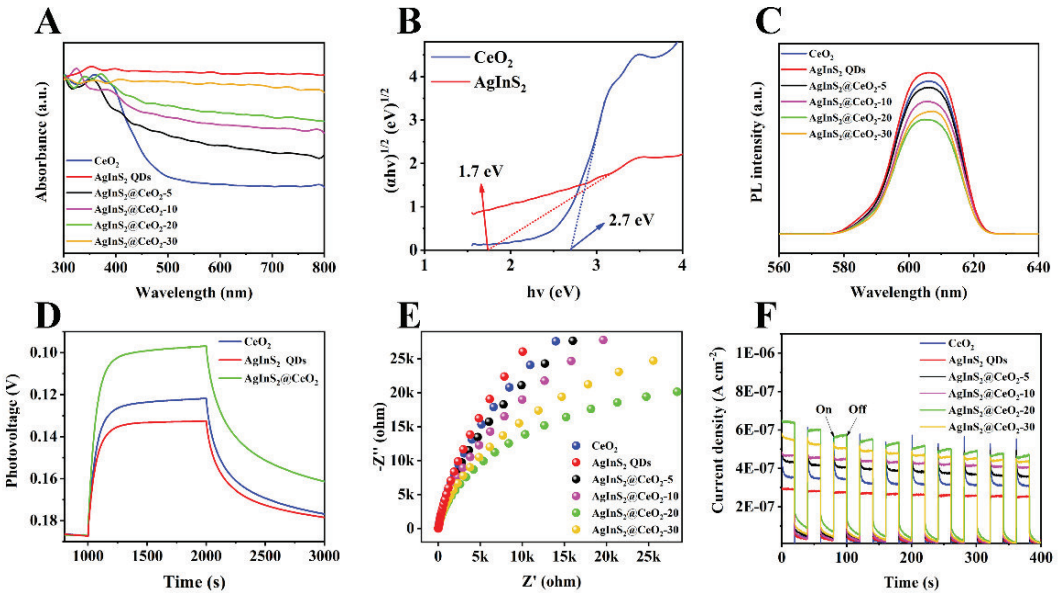

Fig. 4. The UV-vis DRS of CeO_2, $AgInS_2$ QDs, and $AgInS_2$@CeO_2-x (A). The plots of the transformed Kubelka-Munk function versus photo energy for CeO_2 and $AgInS_2$ QDs (B). The PL spectra of CeO_2, $AgInS_2$ QDs, and $AgInS_2$@CeO_2-x (C). The OCVD of CeO_2, $AgInS_2$ QDs, and $AgInS_2$@CeO_2-20 The EIS curves (E) and photocurrent response plots (F) of CeO_2, $AgInS_2$ QDs, and $AgInS_2$@CeO_2-x.

To evaluate the light absorption characteristics of the prepared samples, ultraviolet-visible diffuse reflectance absorption spectra (UV-vis DRS) were employed. As exhibited in Fig. 4A, the absorption edge of CeO_2 is observed at approximately 560 nm. After introducing $AgInS_2$ QDs, an evident redshift of the absorption edge is

observed in $AgInS_2$@CeO_2-x, indicating that the introduction of $AgInS_2$ QDs improves the absorption of photocatalysts in the visible light and near-infrared region. Notably, $AgInS_2$@CeO_2-20 can capture light at all wavelengths. The bandgaps of CeO_2 and $AgInS_2$ QDs are calculated as 2.7 eV and 1.7 eV from plots of the transformed Kubelka-Munk function versus photo energy (Fig. 4B). As we known, charge recombination hinders photo-generated h^+-e^- pairs from effectively participating in the redox reaction, significantly impeding photocatalytic processes. Steady-state photoluminescence (PL) spectroscopy was carried out to investigate charge recombination. As depicted in Fig. 4C, the PL intensity of $AgInS_2$@CeO_2-20 is the lowest among all sample, indicating the weakest charge recombination [45]. As shown in Fig. S5, the oxygen vacancies of CeO_2 generate electron trapping states during the photocatalytic process [46]. The trap states can form more easily due to the presence of oxygen vacancies, which can trap a portion of excited electrons to partially inhibit direct recombination of the photogenerated carriers. As shown in the open-circuit voltage decay (OCVD) in Fig. 4D, $AgInS_2$@CeO_2-20 exhibits the strongest photo-voltage and slowest photovoltage decay, indicating the highest carrier concentration and longest carrier lifetime. In the photocatalytic process, a long carrier lifetime enables photo-generated h^+-e^- pairs to come into more extensive contact with the reactants. To investigate the charge transfer in each photocatalyst, electrochemical impedance spectroscopy (EIS) was carried out. As displayed in Fig. 4E, the impedance of all $AgInS_2$@CeO_2-x samples is lower than that of CeO_2 and $AgInS_2$ QDs after combing $AgInS_2$ QDs. Moreover, $AgInS_2$@CeO_2-20 shows the lowest impedance, indicating that an S-scheme heterojunction is

beneficial for carrier transfer. As shown in the transient photocurrent response plot (Fig. 4F), a similar result with the EIS can be observed. The photocurrent intensity of $AgInS_2$@CeO_2-20 is 1.8 and 2.2 times higher than that of CeO_2 and $AgInS_2$ QDs, respectively, confirming rapid carrier separation under the positive influence of S-scheme heterojunctions.

3.3 Photocatalytic activity of $AgInS_2$@CeO_2-x.

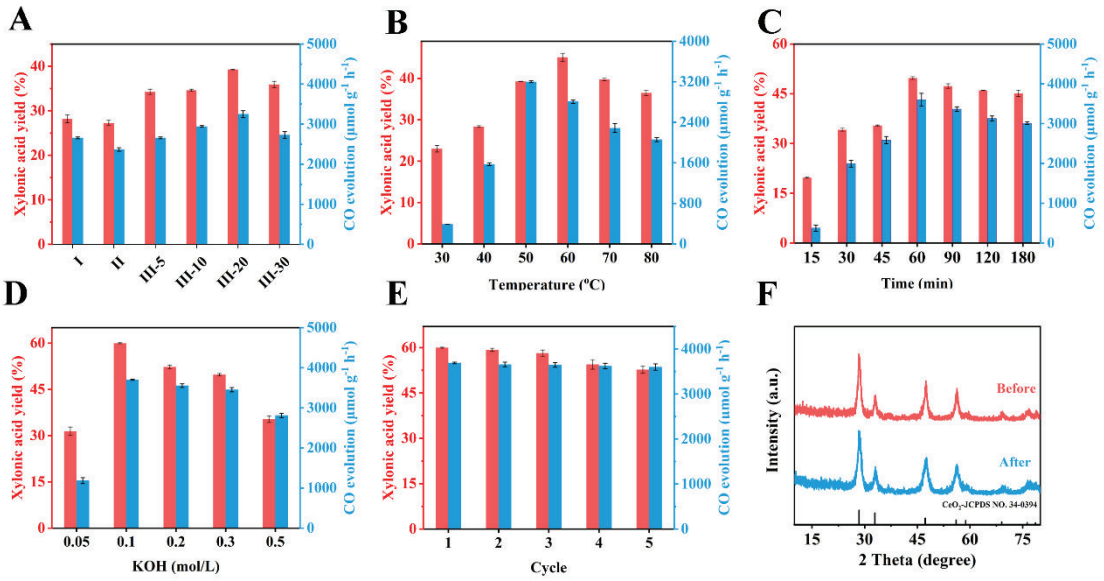

Fig. 5. (A) The photocatalytic conversion of xylose using different samples under visible light irradiation (xylose: 200 mg, samples: 10 mg, KOH solution: 0.30 M, 20 mL, irradiation time: 3 h, reaction temperature: 50 °C). Notes: I: CeO_2; II: $AgInS_2$ QDs; III: $AgInS_2$@CeO_2-5, 10, 20, and 30. The effects of reaction temperatures (B) (xylose: 200 mg, $AgInS_2$@CeO_2-20: 10 mg, KOH solution: 0.3 M, 20 mL, irradiation time: 3 h), irradiation time (C) (xylose: 200 mg, $AgInS_2$@CeO_2-20: 10 mg, KOH solution: 0.30 M, 20 mL, reaction temperature: 60 °C) and KOH concentrations (D) (xylose: 200 mg, $AgInS_2$@CeO_2-20: 10 mg, irradiation time: 1 h, reaction temperature: 60 °C) on the co-production of CO and xylonic acid. (E) The recycling test (xylose: 200 mg, $AgInS_2$@CeO_2-20: 10 mg, irradiation time: 1 h, reaction temperature: 60 °C, KOH solution: 0.1 mol/L). (F) The XRD patterns of fresh and recycled $AgInS_2$@CeO_2-20.

The photocatalytic performance of CeO_2, $AgInS_2$ QDs, and $AgInS_2$@CeO_2-x was

assessed under visible light irradiation. Initially, the photocatalytic performances of various photocatalysts were compared in a 0.3 M KOH solution at 50 °C for 3 h. Fig. 5A shows that the xylonic acid yield and CO evolution rate tends to increase with the addition of different photocatalyst. To determine the optimal reaction parameters, the effects of reaction temperature, reaction time, and alkali concentration were investigated. Fig 5B displays the impact of reaction temperature, with the highest yield (45.1%) of xylonic acid obtained at 60 °C. The CO evolution rate displayed a volcano-like trend, reaching the highest value of 3199.4 μmol g^{-1} h^{-1} at 50 °C. However, at high temperature, lactic acid and other by-productions were released in significant quantities due to the overoxidation of xylonic acid (Fig. S6B). In addition, the reaction under dark conditions was performed (Fig. S7). The yield of xylonic acid was only 32.9% and CO production of only 1625.26 μmol g^{-1} h^{-1} at 60 °C in the dark, indicating a possible minor photothermal process [47]. Noteworthy, photocatalysis is the dominating process to ensure highly efficient productions of xylonic acid and CO, proving the superior photocatalytic performance of the as-developed S-scheme heterojunction. The yield of xylonic acid and CO evolution rate exhibited similar trends (Fig. 5C). The maximum values for the xylonic acid yield and CO evolution rate were 49.7% and 3601.8 μmol g^{-1} h^{-1} at 60 min, respectively, before gradually decreasing. With increasing reaction time, the production of by-products increased, like because xylonic acid was degraded into small molecular products (Fig. S6C). Finally, the influences of alkali concentration in the reaction system were investigated. The xylonic acid yield reached its peak at 60.0% in 0.1 M KOH (Fig. 5D). In system with high alkali concentration, an excess of ·OH radicals may oxidize xylonic acid into other organic acid, leading to a reduction in yield (Fig. S6D). Similarly, CO showed the highest evolution rate (3689.9 μmol g^{-1} h^{-1}) in 0.1 M KOH solution. Notably, the yield of xylonic acid (60.0%) using $AgInS_2$@CeO_2-20 was 3.2 times higher than that in a photocatalyst-free system (18.9%), implying the indispensable role of the $AgInS_2$@CeO_2-20 photocatalyst (Fig. S7). Moreover, the $AgInS_2$@CeO_2-20 photocatalyst exhibited good cycling stability over five consecutive photocatalytic cycles and no significant change in chemical composition (Fig. 5E and 5F). As shown in Fig. S8, electron paramagnetic resonance (EPR) technology was

employed. Both the fresh and recycled $AgInS_2$@CeO_2-20 sample exhibited EPR signals centered at g = 2.003, despite the slightly decreased peak intensity upon recycling. This result suggests excellent stability of $AgInS_2$@CeO_2-20.

3.4 Catalytic Mechanism of $AgInS_2$@CeO_2-x.

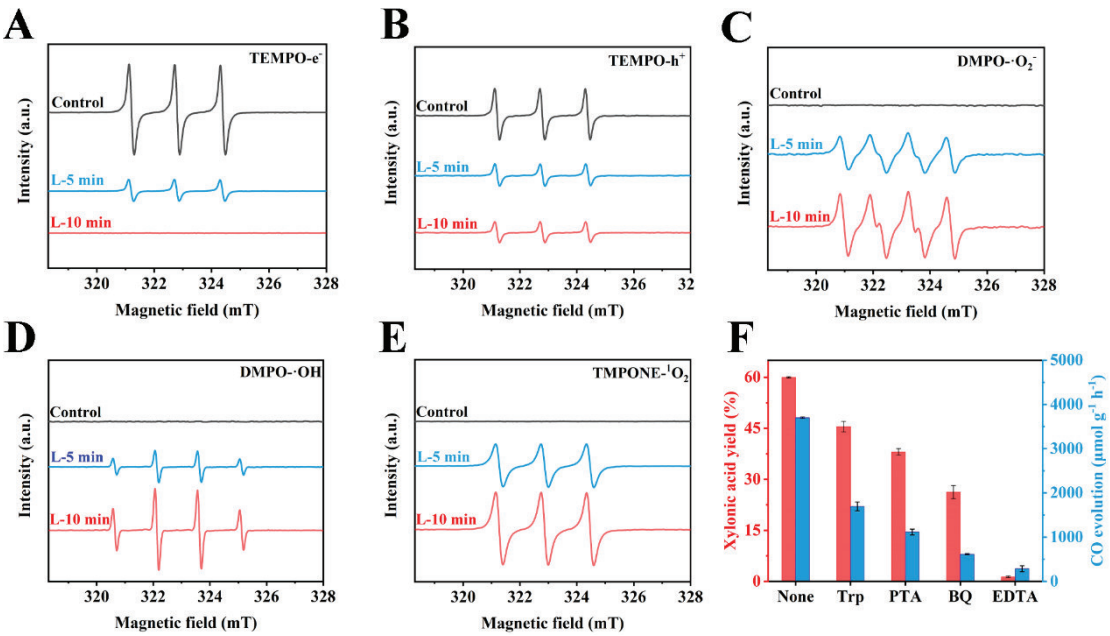

Fig. 6. TEMPO ESR spin-labelling of e^- (A) and h^+ (B), DMPO ESR spin-labelling of $\cdot O_2^-$ (C) and ·OH (D), TEMPONE ESR spin-labelling of $^1O_2$ (E). The effects of different oxidation active species on the co-production of xylonic acid and CO from xylose through $AgInS_2$@CeO_2-20 photocatalysis (F).

To detect the radicals generated during the reaction and assess the redox capabilities of $AgInS_2$@CeO_2-20, ESR characterizations were performed. Three capture agents were used to prove the existence of photo-generated e^-, h^+, $\cdot O_2^-$, ·OH, and $^1O_2$ in the ESR spectrum of $AgInS_2$@CeO_2-20. 2,2,6,6-tetramethylpiperidine-*N*-oxyl (TEMPO) was employed to capture e^- and h^+. As shown in Fig. 6A and 6B, the TEMPO signals weakened with increasing irradiation time, suggesting the presence of e^- and h^+. Similarly, the capture agents 5,5-dimethyl-1-pyrroline-*N*-oxide (DMPO) were utilized to detect the generation of $\cdot O_2^-$ and ·OH. Under light and catalyst conditions, the signals of DMPO-$\cdot O_2^-$ and DMPO-·OH adducts appeared and increased. The DMPO-$\cdot O_2^-$ signal was observed, and the signal intensity was 1:1:1:1 (Fig. 6C and 6D).

Additionally, the signal intensity of DMPO-·OH was 1:2:2:1. These results suggest that $\cdot O_2^-$ and ·OH are produced in the system with $AgInS_2$@CeO_2-20 under light irradiation. Similarly, 2,2,6,6-tetramethyl-4-piperldone-1-oxyl (TEMPONE) was used as a capture agent to detect $^1O_2$. Triplet peaks with equal intensity appeared under light irradiation, indicating the presence of $^1O_2$ in the system (Fig. 6E). A poisoning experiment was conducted to assess the impact of active oxidation species. Various sacrificial agents (e.g. Trp, PTA, BQ, EDTA) were employed to remove these species. As shown in Fig. 6F, the introduction of these sacrificial agents resulted in changes in the yield of xylonic acid and CO evolution rate: 45.5%/1696.4 μmol g^{-1} h^{-1} (Trp), 38.1%/1116.7 μmol g^{-1} h^{-1} (TPA), 26.2%/614.7 μmol g^{-1} h^{-1} (BQ), 1.3%/286.1 μmol g^{-1} h^{-1} (EDTA). These results suggest that the influence of h^+ is greater than those of $^1O_2$, ·OH, and O_2^-.

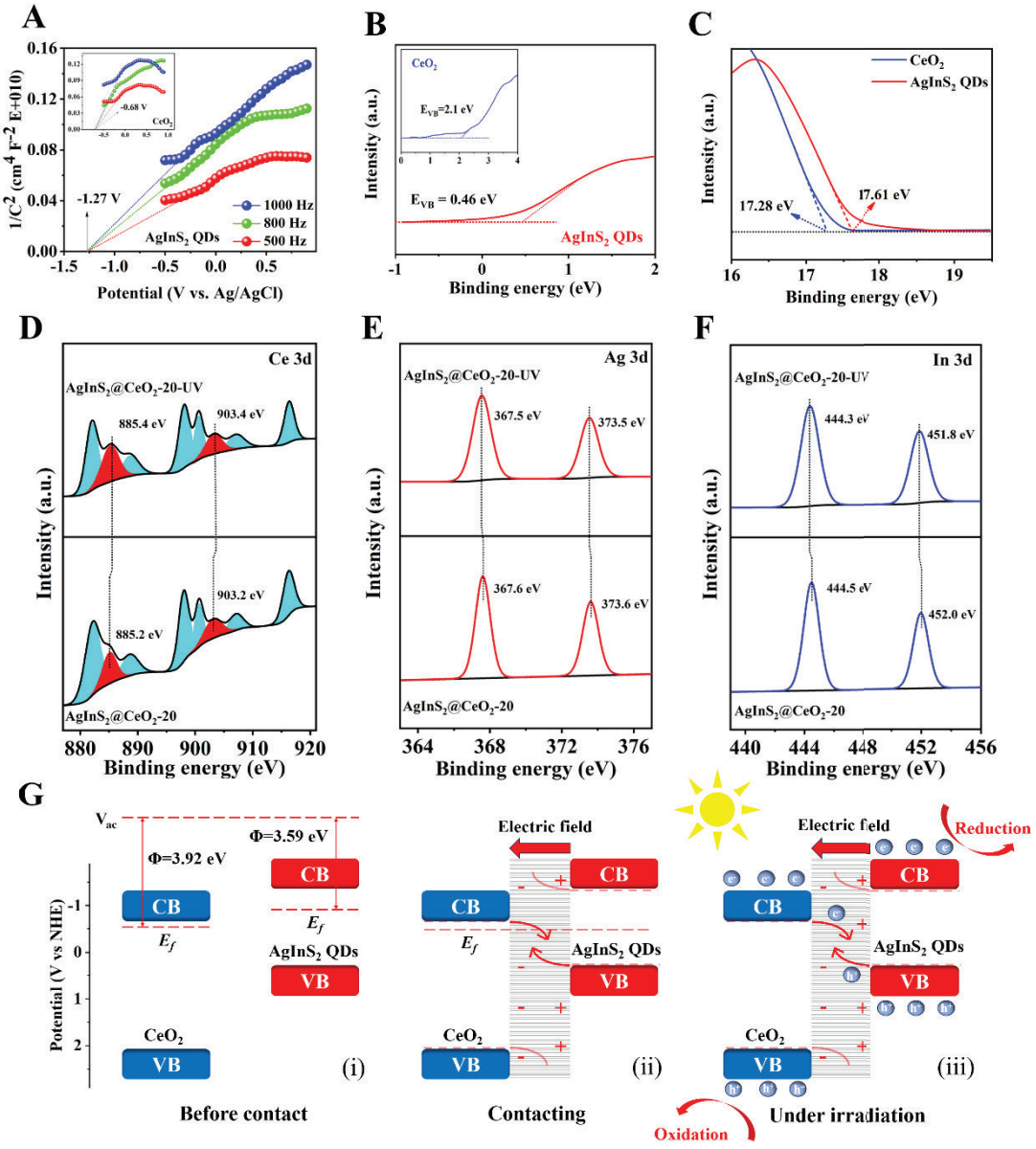

Fig. 7. The M-S plots (A), the valence band spectrum (B), and UPS (C) of CeO_2 and $AgInS_2$ QDs. The High-resolution XPS (In-situ) spectra of Ce 3d (D), Ag 3d (E), and In 3d (F) in the $AgInS_2$@CeO_2-20. The schematic illustration of the S-scheme charge transfer mechanism of $AgInS_2$@CeO_2-x heterostructure.

In this study, the Mott-Schottky (M-S) analysis was employed to determine the conduction band (CB) energy level. The flat band potentials of $AgInS_2$ QDs and CeO_2 were -1.27 and -0.68 V vs. Ag/AgCl, respectively (Fig. 7A). The positive slopes of $AgInS_2$ QDs and CeO_2 indicated that they were both n-type semiconductors. For n-type semiconductors, the flat band potential was positive 0.2 V as compared with CB. Thus, the CBs of $AgInS_2$ and CeO_2 were -1.27 V and -0.68 V vs. normal hydrogen electrode

(NHE), respectively, using the Nernst formula ($E_{NHE} = E_{Ag/AgCl} + 0.197$, pH = 7). The valence band (VB) position was determined through VB-XPS analysis. As displayed in Fig 7B, the VBs of CeO_2 and $AgInS_2$ QDs were 2.1 V and 0.46 V, respectively. The work function (Φ) of semiconductors was calculated using ultraviolet photoelectron spectroscopy (UPS). Fig 7C revealed that the Φ of $AgInS_2$ QDs and CeO_2 were calculated to be 3.59 eV (= 21.20 - 17.61 eV) and 3.92 eV (= 21.20 - 17.28 eV), respectively, with 21.20 eV being the energy of UV excitation. Meanwhile, the Fermi level (E_f) can be calculated using the formula: (E_f = Φ - 4.44 eV), where 4.44 eV is the difference between the vacuum level and NHE. Thus, the E_f of $AgInS_2$ QDs and CeO_2 are calculated to -0.85 V and -0.52 V vs. NHE. Therefore, the staggered band structure of CeO_2 and $AgInS_2$ QDs is depicted in Fig. 7G (i). As compared with CeO_2, $AgInS_2$ QDs have a higher Φ, indicating its stronger ability to bind electrons (e^-). The carrier migration path was investigated via the *ex-situ* and *in-situ* XPS analysis. According to the *ex-situ* XPS results (Fig. 3A and D-F), the binding energies of Ce 3d shifted negatively, while the binding energy of Ag 3d, In 3d, and S 2p shifted positively, suggesting that carriers in $AgInS_2$ QDs flowed to CeO_2 until E_f is balanced. These results in the positive and negative charge accumulation around the interface of $AgInS_2$ QDs and CeO_2, respectively, leading to the presence of an internal electric field. Furthermore, the band edges of $AgInS_2$ QDs and CeO_2 bend upwards and downwards (Fig. 7G (ii)), respectively. As shown in Fig. 7D-F, under UV lamp irradiation, the binding energies of Ag 3d, In 3d, and Ce 3d shifted negatively and positively, respectively, indicating that carriers migrate from CeO_2 to $AgInS_2$ QDs. Under light irradiation, the photo-generated e^- in the CB of CeO_2 recombines with the holes in the VB of $AgInS_2$ QDs. As a result, highly reducing e^- in the CB of $AgInS_2$ QDs and highly oxidizing h^+ in the VB of CeO_2 are retained, participating in reactions on the surface of the photocatalyst (Fig. 7G (iii)). The Kelvin probe force microscope (KPFM) and atomic force microscope (AFM) were used to further verify the existence of an interfacial electric field and the direction of electron transfer in $AgInS_2$@CeO_2-x. As shown in Fig. S9A and S9B, the morphology of $AgInS_2$@CeO_2-x was basically not affected by visible light irradiation. The surface potential difference between $AgInS_2$

QDs (point a) and CeO_2 (point b) was about 51 mV in the dark (Fig. S9C), indicating the formation of an interface electric field from point a to point b. Furthermore, the potential of point a in dark is -393 mV, which declines to -435 mV under the lights (Fig. S9E). The decrease (42 mV) of point a ($AgInS_2$ QDs) was much than that (13 mV) of point b (CeO_2) indicating the migration of photogenerated electrons from CeO_2 to $AgInS_2$ QDs [48]. This results further evidenced the formation of the S-scheme heterostructure between them. In summary, all the results confirm the formation of an S-scheme heterojunction in $AgInS_2$@CeO_2-x.

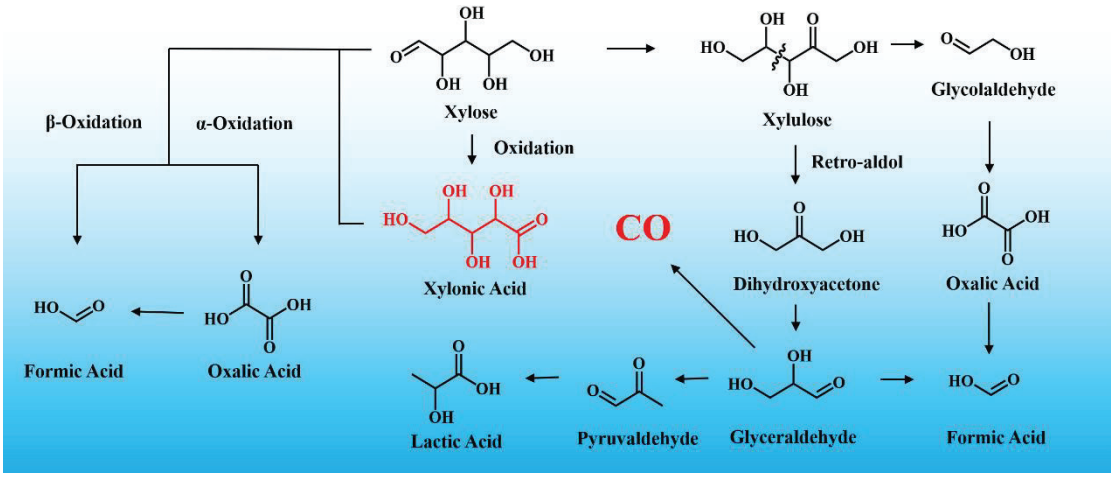

Fig. 8. The possible reaction pathway for photocatalytic co-production of xylonic acid and CO in xylose-alkaline system through $AgInS_2$@CeO_2-20 photocatalysis.

According to previous reports [49], a possible conversion mechanism for xylose on $AgInS_2$@CeO_2-x was proposed (Fig. 8). Initially, under visible light irradiation, e^- transition from the VB to the CB of $AgInS_2$@CeO_2-x, resulting in the formation of h^+-e^- pairs. Subsequently, these h^+-e^- pairs actively contribute to the generation of reactive oxygen species. The mechanism can be summarized as follows:

$$AgInS_2@CeO_2\text{-x} + h\nu \rightarrow e^- + h^+$$

$$O_2 + e^- \rightarrow \cdot O_2^-$$

$$OH^- + h^+ \rightarrow \cdot OH$$

$$\cdot O_2^- + h^+ \rightarrow {}^1O_2$$

It is clear that CeO_2 is the main reactive active center in the photocatalytic selective oxidation of xylose for the co-production of xylonic acid and CO. Firstly, the staggered band structures (Fig. 7G) of CeO_2 and $AgInS_2$ QDs were confirmed through Mott-Schottky (M-S) analysis, valence band spectrum, and ultraviolet photoelectron spectroscopy (UPS). CeO_2 served as an oxidation photocatalyst (OP) in an $AgInS_2$@CeO_2-x S-scheme heterojunction due to a more positive valence band position. Under light irradiation, the photo-generated e^- exists in the CB of CeO_2 and holes manifest in the VB of $AgInS_2$ QDs. As a result, highly reducing e^- in the CB of $AgInS_2$ QDs and highly oxidizing h^+ in the VB of CeO_2 are retained, participating in reactions on the surface of the photocatalyst. Furthermore, various scavengers were injected to remove the oxidation active species, specifically, Trp for $^1O_2$, PTA for ·OH, BQ for $\cdot O_2^-$, and EDTA for h^+ in poisoning experiments. As shown in Fig. 6F, the yield of xylonic acid was trace (1.3%) and the CO evolution was 286.1 μmol g^{-1} h^{-1}, indicating that h^+ played an important role in the selective oxidation of xylose. Finally, the large number of oxygen vacancies in CeO_2 was confirmed by XPS spectra and EPR spectra in this work. Under the positive influence of fast carrier separation and oxygen vacancies, the yield of xylonic acid and CO evolution was greatly increased. In summary, we consider CeO_2 as the main reactive active site in the reaction of selective oxidation of xylose for the co-production of xylonic acid and CO.

Regarding xylonic acid, it is considered the initial product resulting from the selective oxidation of xylose. Simultaneously, xylose and the generated xylonic acid undergo peroxidation to give oxalic acid through α-oxidation. Additionally, β-oxidation yield formic acid. Ultimately, partial formic acid was generated from oxalic acid. Furthermore, xylose can partly isomerize into xylulose, after which glycolaldehyde and dihydroxyacetone are formed through the cleavage of the C-C bond. These compounds then further transform into glycolaldehyde and glyceraldehyde. Subsequently, glyceraldehyde gives rise to CO and formic acid. Lactic acid is produced through the hydration process of pyruvaldehyde.

4. Conclusions

In conclusion, we successfully load $AgInS_2$ QDs onto CeO_2 to form S-scheme heterojunction and enhance oxygen defects via two-step hydrothermal and mild annealing processes. XPS and EPR analysis confirm the increase in oxygen vacancies. The E_f calculation, situ irradiated XPS results, and Kelvin probe force microscopy (KPFM) spectra confirm the S-scheme mechanism in $AgInS_2$@CeO_2-20. The $AgInS_2$@CeO_2-20 photocatalyst showed excellent performance (60.0% xylonic acid yield and 3689.9 μmol g^{-1} h^{-1} CO evolution rate) at 60 ºC in 0.1 M KOH under visible light irradiation, which are much higher than CeO_2 and $AgInS_2$ QDs. ESR results and poisoning experiments indicate the generation of reactive oxygen species and major role of h^+. The possible pathways for the conversion of xylose to CO and xylonic acid have been proposed. This work provides a potential strategy to develop defects rich S-scheme photocatalysts for co-product xylonic acid and CO via biorefinery.

Declaration of Competing Interest

The authors report no declarations of interest.

Acknowledgements

This work was supported by the National Natural Science Foundation of China (22008018, 22378035), Youth Talent Promotion Project of China Association for Science and Technology (YESS20210216), Dalian Outstanding Young Scientific and Technological Talents (2022RY24), Liaoning Province's "Xingliao Talent Plan" Youth Top Talents (XLYC2203010).

Appendix A. Supplementary data

Supplementary material related to this article can be found, in the online version.

References:

[1] V. S. Sikarwar, M. Zhao, P. Clough, J. Yao, X. Zhong, M. Z. Memon, N. Shah, E. J. Anthony, P. S. Fennell, An overview of advances in biomass gasification, *Energy Environ. Sci.*, 9 (2016) 2939-2977.

[2] R. Fang, A. Dhakshinamoorthy, Y. W. Li, H. Garcia, Metal organic frameworks for biomass conversion, *Chem. Soc. Rev.*, 49 (2020) 3638-3687.

[3] J. S. M. Samec, Holistic approach for converting biomass to fuels, *Chem*, 4 (2018) 1199-1200.

[4] J. H. Xu, L. L. Wang, L. J. Sun, W. K. Wang, T. T. Kong, H. P. Jiang, Q. Q. Liu, Boosting photocatalytic synchronous production of H_2 coupled with acetone over Co doped Cu_3P quantum dots/$ZnIn_2S_4$ nanosheets p-n nanojunction, *J. Colloid. Interf. Sci*, 646 (2024) 254-264

[5] M. Wang, M. J. Liu, J. M. Lu, F. Wang, Photo splitting of bio-polyols and sugars to methanol and syngas, *Nat. Commun.*, 11 (2020) 1083.

[6] M. Wang, H. R. Zhou, F. Wang, Photocatalytic production of syngas from biomass, *Acc. Chem. Res.*, 56 (2023) 1057-1069.

[7] J. Lee, S. Jung, Y.T. Kim, H. J. Kim, K. H. Kim, Catalytic and electrocatalytic conversion of glucose into value-added chemicals, *Renew. Sus.t Energ. Rev*, 181 (2023) 113337.

[8] M. S. Lekshmi Sundar, K. Madhavan Nampoothiri, An overview of the metabolically engineered strains and innovative processes used for the value addition of biomass derived xylose to xylitol and xylonic acid, *Bioresour. Technol.*, 345 (2022) 126548.

[9] M. S. Li, L. X. Zhong, W. Chen, Y. M. Huang, Z. X. Chen, D. Q. Xiao, R. Zou, L. Chen, Q. Hao, Z. H. Liu, R. C. Sun, X. W. Peng, Regulating the electron–hole separation to promote selective oxidation of biomass using ZnS@Bi_2S_3 nanosheet catalyst, *Appl. Catal. B-Environ.*, 292 (2021) 120180.

[10] A. B. Bañares, G. M. Nisola, K. N. G. Valdehuesa, W. K. Lee, W. J. Chung, Understanding D-xylonic acid accumulation: a cornerstone for better metabolic engineering approaches, *Appl. Microbiol. Biotechnol.*, 105 (2021) 5309-5324.

[11] K. N. Liu, J. L. Ma, X. P. Yang, D. N. Jin, Y. C. Li, G. J. Jiao, S. Q. Yao, S. L. Sun, R.C. Sun, Boosting electron kinetics of anatase TiO_2 with carbon nanosheet for efficient photo-reforming of xylose into biomass-derived organic acids, *J. Alloys Compd.*, 906 (2022) 164276.

[12] J. Q. Zhang, K. N. Liu, S.L. Sun, R. C. Sun, J. L. Ma, Photo-splitting xylose and xylan to xylonic acid and carbon monoxide, *Green Chem.*, 24 (2022) 8367-8376.

[13] C. W. Sun, H. Li, L. Q. Chen, Nanostructured ceria-based materials: synthesis, properties, and applications, *Energy Environ. Sci.*, 5 (2012) 8475-8505.

[14] Y. C. Zhang, Z. Li, L. Zhang, L. Pan, X. W. Zhang, L. Wang, A. Fazal e, J. J. Zou, Role of oxygen vacancies in photocatalytic water oxidation on ceria oxide: Experiment and DFT studies, *Appl. Catal. B-Environ.*, 224 (2018) 101-108.

[15] S. M. Fang, Y. J. Xin, L. Ge, C. C. Han, P. Qiu, L. E. Wu, Facile synthesis of CeO_2 hollow structures with controllable morphology by template-engaged etching of Cu_2O and their visible light photocatalytic performance, *Appl. Catal. B-Environ.*, 179 (2015) 458-467.

[16] X. Huang, K. Zhang, B. Peng, G. Wang, M. Muhler, F. Wang, Ceria-Based Materials for Thermocatalytic and Photocatalytic Organic Synthesis, *ACS Catal.*, 11 (2021) 9618-9678.

[17] Y. Q. Lu, H. Deng, T. T. Pan, X. Liao, C. B. Zhang, H. He, Effective toluene qzonation over δ-MnO_2: oxygen vacancy-induced reactive oxygen species, *Environ. Sci. Technol.*, 57 (2023) 2918-2927.

[18] S. Wei, H. X. Zhong, H. T. Wang, Y. J. Song, C. M. Jia, M. Anpo, L. Wu, Oxygen vacancy enhanced visible light photocatalytic selective oxidation of benzylamine over ultrathin Pd/BiOCl nanosheets, *Appl. Catal. B-Environ.*, 305 (2022) 121032.

[19] C. H. Shen, Y. Chen, X. J. Xu, X. Li, X. J. Wen, Z. T. Liu, R. Xing, H. Guo, Z. H. Fei, Efficient photocatalytic H_2 evolution and Cr(VI) reduction under visible light using a novel Z-scheme $SnIn_4S_8/CeO_2$ heterojunction photocatalysts, *J. Hazard. Mater.*, 416 (2021) 126217.

[20] Y. F. Wang, L. Yang, R. Zou, J. W. Lan, A. R. Yao, H. Y. Xiao, S. J. Lin, Z-scheme CeO_2/Ag/CdS heterojunctions functionalized cotton fibers as highly recyclable and efficient visible light-driven photocatalysts for the degradation of dyes, *J. Clean. Prod*, 380 (2022) 135012.

[21] Y. Shi, L. Li, Z. Xu, F. Guo, W. Shi, Construction of full solar-spectrum available S-scheme heterojunction for boosted photothermal-assisted photocatalytic H_2

565 production, *Chem. Eng. J*, 459 (2023) 141549.
566 [22] Q. L. Xu, L. Y. Zhang, B. Cheng, J. J. Fan, J. G. Yu, S-scheme heterojunction
567 photocatalyst, *Chem*, 6 (2020) 1543-1559.
568 [23] X. W. Ruan, C. X. Huang, H. Cheng, Z. Q. Zhang, Y. Cui, Z. Y. Li, T. F. Xie, K.
569 K. Ba, H. Y. Zhang, L. Zhang, X. Zhao, J. Leng, S. Y. Jin, W. Zhang, W. T. Zheng, S.
570 K. Ravi, Z. F. Jiang, X. Q. Cui, J. G. Yu, A twin S-scheme artificial photosynthetic
571 system with self-assembled heterojunctions yields superior photocatalytic hydrogen
572 evolution rate, *Adv. Mater*, 35 (2023) 2209141.
573 [24] L.Y. Zhang, J. J. Zhang, H. G. Yu, J. G. Yu, Emerging S-scheme photocatalyst,
574 *Adv. Mater*, 34 (2022) 2107668.
575 [25] L. Zhao, J. Bian, X. Zhang, L. Bai, L. Xu, Y. Qu, Z. Li, Y. Li, L. Jing, Construction
576 of ultrathin S-scheme heterojunctions of single Ni atom immobilized Ti-MOF and
577 $BiVO_4$ for CO_2 photoconversion of nearly 100% to CO by pure water, *Adv. Mater*., 34
578 (2022) 2205303.
579 [26] Y. You, S. X. Chen, J. Zhao, J.F. Lin, D. L. Wen, P. Z. Sha, L. B. Li, D. L. Bu, S.
580 M. Huang, Rational design of S-scheme heterojunction towards efficient photocatalytic
581 cellulose reforming for H_2 and formic acid in pure water, *Adv. Mater*, (2023), doi:
582 https://doi.org/10.1002/adma.202307962.
583 [27] M. C. Nevárez Martínez, B. Bajorowicz, T. Klimczuk, A. Żak, J. Łuczak, W.
584 Lisowski, A. Zaleska-Medynska, Synergy between $AgInS_2$ quantum dots and ZnO
585 nanopyramids for photocatalytic hydrogen evolution and phenol degradation, *J. Hazrd.*
586 *Mater*, 398 (2020) 123250.
587 [28] J. G. Du, S. L. Ma, H. P. Liu, H. C. Fu, L. Li, Z. Q. Li, Y. Li, J. G. Zhou, Uncovering
588 the mechanism of novel $AgInS_2$ nanosheets/TiO_2 nanobelts composites for
589 photocatalytic remediation of combined pollution, *Appl. Catal. B-Environ*, 259 (2019)
590 118062.
591 [29] P. Sun, Z. P. Xing, Z. Z. Li, W. Zhou, Recent advances in quantum dots
592 photocatalysts, *Chem. Eng. J*, 458 (2023) 141399.
593 [30] K. L. Zhang, M. Zhou, K. Yang, C. L. Yu, P. Mu, Z. Z. Yu, K. Q. Lu, W. Y. Huang,
594 W.X. Dai, Photocatalytic H_2O_2 production and removal of Cr (VI) via a novel Lu_3NbO_7:

595 Yb, Ho/CQDs/$AgInS_2$/In_2S_3 heterostructure with broad spectral response, *J. Hazard.*
596 *Mater*, 423 (2022) 127172.
597 [31] Y. Zhao, X. Fan, H. Zheng, E. Liu, J. Fan, X. Wang, Bi_2WO_6/$AgInS_2$ S-scheme
598 heterojunction: Efficient photodegradation of organic pollutant and toxicity evaluation,
599 *J. Mater. Sci Technol.*, 170 (2024) 200-211.
600 [32] L. Wang, R. Sa, Y. Wei, X. Ma, C. Lu, H. Huang, E. Fron, M. Liu, W. Wang, S.
601 Huang, J. Hofkens, M. B. J. Roeffaers, Y. J. Wang, J. Wang, J. Long, X. Fu, R. Yuan,
602 Near-infrared light-driven photoredox catalysis by ttransition-metal-complex nanodots,
603 *Angew. Chem. Int. Ed.*, 61 (2022) e202204561.
604 [33] L. Zhang, L. Zhang, G. C. Xu, C. Zhang, X. Li, Z. P. Sun, D. Z. Jia, Low-
605 temperature CO oxidation over CeO_2 and CeO_2@Co_3O_4 core-shell microspheres, *New.*
606 *J. Chem*, 41 (2017) 13418-13424.
607 [34] X. Y. Gu, C. Tan, L. X. He, J. Guo, X. Zhao, K. Z. Qi, Y. Yan, Mn^{2+} doped $AgInS_2$
608 photocatalyst for formaldehyde degradation and hydrogen production from water
609 splitting by carbon tube enhancement, *Chemosphere*, 304 (2022) 135292.
610 [35] J. Jin, J. G. Yu, D. P. Guo, C. Cui, W. Ho, A hierarchical Z-Scheme CdS-WO_3
611 photocatalyst with enhanced CO_2 reduction activity, *Small*, 11 (2015) 5262-5271.
612 [36] X. Q. Wang, J. L. Wu, J. L. Wang, H. L. Xiao, B. X. Chen, R. Peng, M. L. Fu, L.
613 M. Chen, D. Q. Ye, W. Wen, Methanol plasma-catalytic oxidation over CeO_2 catalysts:
614 Effect of ceria morphology and reaction mechanism, *Chem. Eng. J*, 369 (2019) 233-
615 244.
616 [37] X. Li, W.Q. Fan, Y.J. Bai, Y. Liu, F.F. Wang, H.Y. Bai, W.D. Shi,
617 Photoelectrochemical reduction of nitrate to ammonia over CuPc/CeO_2 heterostructure:
618 Understanding the synergistic effect between oxygen vacancies and Ce sites, *Chem.*
619 *Eng. J*, 433 (2022) 133225.
620 [38] H. L. Tang, T. T. Ju, Y. Dai, M. L. Wang, Y. Q. Ma, M. Wang, G. H. Zheng,
621 Ultrahigh efficiency CH_4 photocatalytic conversion to C1 liquid products over cheap
622 and vacancy-rich CeO_2 at 30 °C, *J. Mater. Chem. A*, 10 (2022) 18978-18988.
623 [39] R. Khatun, R. S. Pal, M. A. Shoeb, D. Khurana, S. Singhl, N. Siddiqui, M. K.
624 Poddar, T. S. Khan, R. Bal, Generation of active oxygen species by CO_2 dissociation

over defect-rich Ni-Pt/CeO_2 catalyst for boosting methane activation in low-temperature dry reforming: Experimental and theoretical study, *Appl. Catal. B-Environ*, 340 (2024) 123243.

[40] R. Khatun, S. Bhandari, M.K. Poddar, C. Samanta, T.S. Khan, D. Khurana, R. Bal, Partial oxidation of methane over high coke-resistant bimetallic Pt-Ni/CeO_2 catalyst: Profound influence of Pt addition on stability, *Int. J. Hydrogen. Energ*, 47 (2022) 38895-38909.

[41] M. Yao, Z. M. Tao, G. B. Liu, S. M. Li, Y. Zhang, A novel calcination method towards layered Ni-rich cathode with enhanced electrochemical performances and regulated oxygen vacancies, *Chem. Eng. J*, 473 (2023) 145090.

[42] J. Z. Qin, X. Hu, X. Y. Li, Z. F. Yin, B. J. Liu, K.-h. Lam, 0D/2D $AgInS_2$/MXene Z-scheme heterojunction nanosheets for improved ammonia photosynthesis of N_2, *Nano Energy*, 61 (2019) 27-35.

[43] W. C. Wang, Y. Tao, J. Fan, Z. Yan, H. Shang, D. L. Phillips, M. Chen, G. Li, Fullerene-Graphene Acceptor Drives Ultrafast Carrier Dynamics for Sustainable CdS Photocatalytic Hydrogen Evolution, *Adv. Funct. Mater* 32 (2022) 2201357.

[44] G. T. Sun, Z. G. Tai, F. Li, Q. Ye, T. Wang, Z. Fang, L. C. Jia, W. Liu, H. Q. Wang, Construction of $ZnIn_2S_4$/CdS/PdS S-scheme heterostructure for efficient photocatalytic H_2 production, *Small*, 19 (2023) 2207758.

[45] Y. Zhang, Y. X. Wu, L. Wan, W. F. Yang, H. J. Ding, C.Y. Lu, W. H. Zhang, Z. P. Xing, Double Z-Scheme g-C_3N_4/BiOI/CdS heterojunction with I^{3-}/I^- pairs for enhanced visible light photocatalytic performance, *Green. Energy. Environ.*, 7 (2022) 1377-1389.

[46] Z. Wei, W. Wang, W. Li, X. Bai, J. Zhao, E.C.M. Tse, D.L. Phillips, Y. Zhu, Steering electron-hole migration pathways using oxygen vacancies in tungsten oxides to enhance their photocatalytic oxygen evolution performance, *Angew. Chem. Int. Ed.*, 60 (2021) 8236-8242.

[47] X. F. Ma, R. Xiao, Y. Wei, S. Zhang, X. Hu, L. Zhang, N. Qin, L. Wang, Z. Ding, H. Lin, Z. Zhang, J. Long, R. Yuan, Photothermal catalytic conversion of water and inert nitriles to amide activated by in-situ formed transition-metal-complex nanodots,

Appl. Catal. B-Environ, 344 (2024) 123636.

[48] T. Ying, W. Liu, L. Yang, S. Zhang, Z. Wu, J. Li, R. Song, W. Dai, J. Zou, S. Luo, S-scheme construction boosts highly active self-supporting CeO_2/Cu_CO photocatalyst for efficient degradation of indoor VOCs, *Sep. Purif. Technol.*, 330 (2024) 125272.

[49] Y. F. Zhang, H. Luo, L.Z. Kong, X. P. Zhao, G. Miao, L.J. Zhu, S. G. Li, Y. H. Sun, Highly efficient production of lactic acid from xylose using Sn-beta catalysts, *Green. Chem*, 22 (2020) 7333-7336.